Physics of the Earth and Planetary Interiors 223 (2013) 21–31

Contents lists available at SciVerse ScienceDirect

Physics of the Earth and Planetary Interiors

journal homepage: www.elsevier.com/locate/pepi

Axisymmetric and non-axisymmetric magnetostrophic MRI modes

Ludovic Petitdemange, Emmanuel Dormy *, Steven Balbus [1]

MAG (ENS/IPGP), LRA, Département de Physique, Ecole Normale Supérieure, Paris, France

ARTICLE INFO

Article history:
Received 31 October 2012
Received in revised form 26 February 2013
Accepted 17 March 2013
Available online 3 April 2013
Edited by C. Jones

Keywords:
Earth core
Magnetohydrodynamics (MHD)
Magnetorotational instability (MRI)

ABSTRACT

The magnetorotational-instability is central to the understanding of many astrophysical magnetohydrodynamic flows (in particular accretion discs). We have recently shown that a modified version of this instability, the magnetostrophic MRI (MS-MRI), is relevant to the dynamics of the Earth liquid core (Petitdemange et al., 2008). Our previous study used a purely axial imposed magnetic field and considered only axisymmetric instabilities. We investigate here the effects of a large scale toroidal magnetic field on the development and saturation of the MS-MRI both in an axisymmetric setup and in fully three-dimensional configurations. We use direct numerical modeling of the full MHD equations (both in the linear and non-linear regimes) in a spherical geometry. We interpret our results using WKB expansions and shearing coordinates. We find that three-dimensional MS-MRI modes exhibit a strong helical structure for parameters relevant to planetary interiors. Three-dimensional MS-MRI modes share some similarities with their axisymmetric counterparts. They are amplified on the same short timescale. When non-linear effects become significant, they act to decrease the shear. During saturation, the magnetic structure expands spatially, while drifting at a constant rate along the direction of the rotation axis. A striking result is that an $m = 1$ mode can dominate in the non-linear regime when a sufficiently large toroidal field is present. Three-dimensional MS-MRI modes could play an important role in planetary interior dynamics. They can cause rapid magnetic field variations and also act to limit the shear in the conducting liquid core.

1. Introduction

The magnetorotational instability (MRI) can develop in the presence of a weak magnetic field in a differentially rotating conducting fluid. It is an essential effect in understanding the dynamics of accretion disks owing to the presence of a strong shear in these objects (see Balbus and Hawley, 1991). It was shown that this instability can also affect the dynamics of planetary interiors (Petitdemange et al., 2008). The rotation properties of planetary interiors obviously differ from those of an accretion disk. To leading order, they correspond to solid body rotation. In addition, the resistive effects are on an equal footing with dynamical processes. The relevant force balance in the Earth core is the so-called "magnetostrophic regime", which allows for the development of a slightly modified version of the classical MRI. We refer to this as the magnetostrophic-MRI or MS-MRI (Petitdemange et al., 2008).

Earlier studies relied on a very simple local model, involving a purely axial background magnetic field and a rotation constant on cylinders. In this study, we investigate the MS-MRI with a more elaborate planetary interior model, in which an additional background toroidal magnetic field is taken into account. We highlight the action of curvature terms associated with background magnetic field lines on both axisymmetric and non-axisymmetric disturbances. Because the shear is weak, curvature terms are on the same footing in this problem as the background gradients of the zonal velocity, introducing yet another essential distinction with accretion disks.

In this manuscript, we do not focus on the origin of the global magnetic fields, but on MHD instabilities induced by the presence of a background shear and a global magnetic field in rapid rotating systems. In contrast to the axial magnetic field geometry considered in Petitdemange et al. (2008), we study here a helical magnetic configuration. This is a somewhat more realistic field geometry, as differential rotation generates azimuthal from poloidal fields (the so called ω-effect). According to Roberts and Gubbins (1986), the toroidal component could exceed the poloidal one by a factor Rm (Rm is the magnetic Reynolds number $Rm = UL/\eta$) in the Earth outer core ($Rm \approx 100$). The belief that the toroidal component largely exceeds the poloidal in planetary interiors, led previous stability analyses to consider only a purely toroidal applied field (see Acheson and Hide, 1973 and Fearn, 1993).

* Corresponding author.
E-mail address: dormy@phys.ens.fr (E. Dormy).
[1] Present address: Astrophysics, Department of Physics, University of Oxford Keble Road, Denys Wilkinson Building, Oxford OX1 3RH, United Kingdom.

0031-9201/$ - see front matter © 2013 Elsevier B.V. All rights reserved.
http://dx.doi.org/10.1016/j.pepi.2013.03.003

2. Formulation

We investigate the stability of a conducting fluid in a rotating sphere subject to a background flow $\mathbf{U_0}$ and field $\mathbf{B_0}$ in a rotating spherical domain. Perturbations are governed by the linearized MHD equations

$$\frac{\partial \mathbf{u}}{\partial t}+(\mathbf{U_0}\cdot\nabla)\mathbf{u}+(\mathbf{u}\cdot\nabla)\mathbf{U_0}+2\mathbf{e_z}\times\mathbf{u}=E\Delta\mathbf{u}-\nabla\pi+\frac{\Lambda E}{Pm}\begin{bmatrix}(\nabla\times\mathbf{B_0})\times\mathbf{b}\\+(\nabla\times\mathbf{b})\times\mathbf{B_0}\end{bmatrix}, \tag{1}$$

$$\frac{\partial \mathbf{b}}{\partial t}=\frac{E}{Pm}\Delta\mathbf{b}+\nabla\times[\mathbf{U}_0\times\mathbf{b}+\mathbf{u}\times\mathbf{B_0}], \tag{2}$$

$$\nabla\cdot\mathbf{b}=0,\qquad \nabla\cdot\mathbf{u}=0, \tag{3}$$

where we introduced the Ekman number, the Elsasser number and the magnetic Prandtl number defined as

$$E=\nu/(\Omega_0 r_o^2),\qquad \Lambda=B_0^2/(\mu\rho_0\eta\Omega_0),\qquad Pm=\nu/\eta. \tag{4}$$

As usual, $\nu,\ \eta,\ \rho_0,\ \mu$ denote the kinematic viscosity, the magnetic resistivity, the density and the magnetic permeability, all assumed to be constant. Where Ω_0 denotes the angular rotation of the outer sphere, which serves as reference frame, and B_0 denotes the magnitude of the axial component of the background magnetic field, constant in time. The background magnetic field considered in this study also includes an azimuthal component. In the above, we used the radius of the spherical domain r_o as unit of length, and $1/\Omega_0$ as unit of time.

We perform direct numerical simulations (DNS) of this system of equations in a spherical geometry using the PaRoDy code (Dormy et al., 1998, and later collaborative developments). We want to stress the presence of the $(\nabla\times\mathbf{B_0})\times\mathbf{b}$ term in the Navier–Stokes equation, as we consider here a more complex background magnetic field than in Petitdemange et al. (2008). We are particularly interested in studying the role of a background helical magnetic field. The magnetic configuration has no cylindrical radial component, and the toroidal applied field is thus time independent. For convenience, we restrict this paper to the study of a toroidal field proportional to s. Such a field reduces the possibility of generating purely magnetic instabilities (see Acheson and Hide, 1973).

The reference state $(\mathbf{U_0},\mathbf{B_0})$ is axisymmetric and has a very simple mathematical form. In all the simulations presented in this paper, the reference velocity field depends only on the radial cylindrical variable $s=r\sin\theta$ as a simple gaussian function

$$\mathbf{U_0}=Ro e^{-(s-1/2)^2/\delta}\mathbf{e}_\phi, \tag{5}$$

where Ro, the Rossby number, is a scalar parameter which measures the importance of the differential rotation. Throughout this work, we have set $\delta=0.015$ (This velocity profile was used previously in Petitdemange, 2010).

The fluid is threaded by the background magnetic field $\mathbf{B_0}$. In contrast to previous numerical investigations, here $\mathbf{B}_0$ has a helical form, i.e. $\mathbf{B_0}=B_0\mathbf{e_z}+B_\phi\mathbf{e}_\phi$ where $(\mathbf{e_s},\mathbf{e}_\phi,\mathbf{e_z})$ denotes the unit vectors in cylindrical coordinates.

Our analysis is restricted to an applied magnetic field having no radial component. The effect of including a radial component in the reference field would obviously be to generate a linear growth in time of the toroidal component. We choose to focus on a steady background toroidal field of the form $B_\phi\propto s=r\sin\theta$, where (r,θ,ϕ) denote spherical coordinates. This spatial form has several advantages. First, it is very simple and allows a direct comparison of numerical results with local analysis carried out in cylindrical coordinates. Second, this magnetic configuration is stable with respect to Acheson-type instabilities (see Acheson and Hide, 1973). Finally, the Lorentz force associated with such a helical field can be easily compensated by a radial pressure gradient (in cylindrical coordinates). This background field has no particular physical basis, and is chosen here primarily for convenience.

Note that, because of diffusion, the reference field is not an exact steady solution of the induction equation. We are interested here, however, in modes growing more rapidly than the diffusion timescale.

Finally, we introduce $\beta=B_\phi(s=1/2)/B_z$ as a measure of the ratio of the toroidal to poloidal applied field.

3. Effect of a toroidal magnetic field on the linear axisymmetric mode

3.1. Numerical simulations

Petitdemange et al. (2008) discussed the particular spatial structure of unstable modes arising from a purely axial background field. These modes have a radial field component b_s that is exactly out of phase by half a period with respect to the azimuthal field b_ϕ. The radial velocity perturbation u_s is a quarter-period ahead of b_ϕ. This result is a hallmark of the MS-MRI mechanism. This phase-shift might allow the possibility of identifying the instability in global direct numerical dynamos, but the action of an additional background toroidal field strongly modifies this phase dependency. u_s is no any longer exactly a quarter-period shifted (see Fig. 1). In addition, we find that the phase drift depends on the dimensionless parameters. The classical picture described above is recovered only in the limit of vanishing Ekman number.

It is well known that the magnetic energy of magnetostrophic waves is much greater than their kinetic energy. In Table 1, the ratio of the magnetic to kinetic energy (hereafter noted R_E) is given for our numerical results. R_E depends on the magnitude of the background toroidal field and on the dimensionless parameters. As expected, it increases when the parameters approach the limit relevant to planetary interior, i.e. small Ekman number E, small magnetic Prandtl number Pm, small magnetic Ekman number E/Pm and Elsasser number Λ of order unity.

We find that in the presence of a strong enough toroidal field, as measured by $Q=\beta E\Lambda/Pm$, the dominance of the magnetic energy over the kinetic energy is suppressed (i.e. R_E decreased).

We observe that the steady instability induced by a purely axial background field becomes an overstability instability in the presence of a helical background field Hollerbach and Rüdiger (2005). The perturbations grow exponentially while propagating along

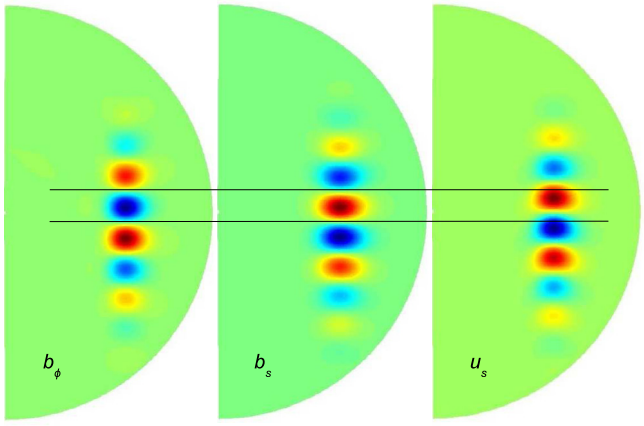

Fig. 1. The most unstable mode in a direct numerical simulation with $E=2.5\times10^{-6}$, $Pm=0.5$, $\Lambda=1$ and $\beta=10$. The applied toroidal magnetic field modifies the MS-MRI mechanism, as illustrated by the fact b_s is not anymore in quadrature with u_s.

Table 1
Numerical axisymmetric results obtained for a helical background field.

2E	*Pm*	2Λ	*β*	*Ro*	IRe(*σ*)	IIm(*σ*)	R_E
2.10^{-5}	0.5	2	15	0.03	0.0325	0.0025	11
	0.5	2	1	0.03	0.0352	0.0003	45
10^{-5}							
	0.5	2	10	0.03	0.0389	0.0009	30
	0.5	1	10	0.03	0.0214	0.00052	67
	0.5	2	1	0.03	0.0401	0.00012	47
	0.5	2	0	0.03	0.0384	0	48
	0.5	2	10	0.01	0.0099	0.00078	45.5
	0.5	2	3	0.01	0.010	0.00025	130
5.10^{-6}							
	0.25	2	3	0.01	0.010	0.00025	122
	0.5	2	10	0.005	0.0050	0.000415	11
	0.25	2	0	0.005	0.0039	0	319
3.10^{-6}	1	1	10	0.03	0.0247	0.00017	83
	0.5	1	10	0.03	0.0226	0.00013	112
	0.5	2	10	0.01	0.0128	0.00025	95
	0.5	2	3	0.01	0.0128	0.00007	151
	0.5	2	1	0.01	0.0126	0.00002	160
	0.25	2	3	0.01	0.0112	0.00015	137
2.10^{-6}							
	0.25	4	3	0.005	0.0081	0.000185	143
	1	2	10	0.005	0.0067	0.00008	221
	0.25	2	10	0.03	0.0428	0.00034	39
	0.25	2	10	0.01	0.0124	0.00031	84
	0.25	2	10	0.005	0.0053	0.00030	109
	0.25	2	3	0.005	0.0053	0.00010	234
	0.25	2	1	0.005	0.0052	0.00003	291
	0.1	2	3	0.005	0.0038	0.00023	170
	0.1	2	1	0.005	0.0038	0.000085	263

the rotation axis in the direction of the Poynting flux (or equivalently in the direction $-\beta\mathbf{e_z}$). For axisymmetric disturbances, the growth rates and wavenumbers do not depend on $\beta = B_\phi(s = 1/2)/B_z$. For $\beta > 0$, perturbations initially located at the top of the sheared domain propagate downwards in the $-z$-direction, with a fixed wave packet structure. Since the unstable domain is enclosed by boundaries, the perturbations have to decay when they reach the lower boundary. However, decreasing the parameter Q reduces the wave velocity (see Fig. 2).

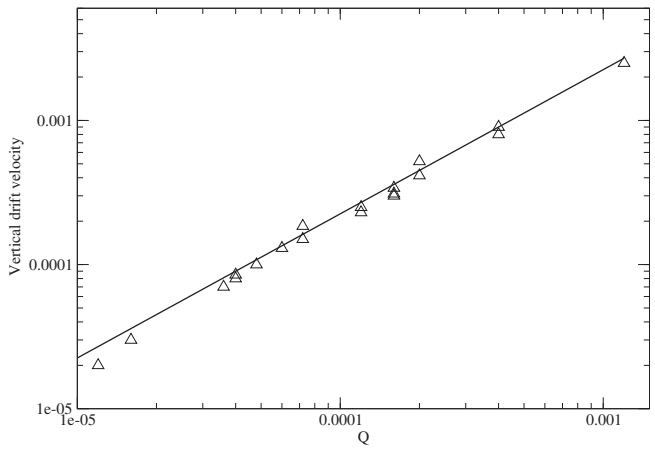

Fig. 2. Each triangle corresponds to one simulation listed in Table 1. Only simulations with $Pm < 1$ have been included in order to compare numerical results with the local description of Section 3.2 (black curve) relevant to small *Pm* numbers. Our prediction $c_z \propto Q \equiv \beta E\Lambda/Pm$ fits the numerical results very well.

3.2. Local description

Acheson and Hide (1973) studied the magnetic instabilities caused by the presence of a pure toroidal magnetic field and a background shear. They performed a local non-axisymmetric linear analysis in the magnetostrophic regime. The pure toroidal magnetic configuration yields only non-axisymmetric unstable modes. As showed in Petitdemange et al. (2008), an axial magnetic field acting on weakly sheared flows allows the development of axisymmetric modes. In this section, we consider axisymmetric disturbances (u_s, u_ϕ, u_z) and (b_s, b_ϕ, b_z).

In an astrophysical context, the curvature terms associated with the toroidal magnetic field are small and usually neglected in local descriptions, though not of course in global simulations (see Balbus and Hawley, 1991, 1998). Local analysis in disks uses approximations suited to the study of short-wavelength perturbations and weak background magnetic fields.

As noted by Acheson and Hide (1973) and Acheson (1978)), these curvature terms are important in stability analysis of planetary interiors. We therefore perform a local description using the WKB approximation in the magnetostrophic regime. We use the streamfunctions Φ and Ψ in order to compare our analysis with the one carried out by Liu et al. (2006) describing HMRI in accretion disks. We therefore introduce

$$(u_s, u_z) = (\partial_z\Phi, -s^{-1}\partial_s(s\Phi)), \qquad (b_s, b_z) = (\partial_z\Psi, -s^{-1}\partial_s(s\Psi)). \tag{6}$$

The linearized MHD equations in the magnetostrophic regime can then be rewritten

$$-2\Omega\partial_z u_\phi = \frac{1}{\mu\rho_0}\left(-2(B_\phi/s)\partial_z b_\phi + B_z\partial_z D\Psi\right), \tag{7}$$

$$2\Omega\partial_z\Phi = \frac{1}{\mu\rho_0}\left(B_z\partial_z b_\phi + \partial_z\Psi(B_\phi/s) + \partial_z\Psi \mathrm{d}_s B_\phi\right), \tag{8}$$

$$(\partial_t - \eta D)\Psi = B_z\partial_z\Phi, \tag{9}$$

$$(\partial_t - \eta D)b_\phi = B_z\partial_z u_\phi - \partial_z\Phi \mathrm{d}_s B_\phi + (B_\phi/s)\partial_z\Phi + s\mathrm{d}_s\Omega\partial_z\Psi, \tag{10}$$

where $D \equiv \partial_s(\partial_s + s^{-1}) + \partial_z^2$.

Contrasting with Liu et al. (2006), no *a priori* radial dependency has been assumed for B_ϕ. We also consider here the magnetostrophic limit, rather than the complete Navier–Stokes equations. This simplifies the calculation. Our results may also be compared with those obtained by Pessah and Psaltis (2005).

Note the presence of two additional terms in (7)–(10) as compared to our earlier study (Petitdemange et al., 2008). These terms involve $\mathrm{d}_s B_\phi$ and B_ϕ/s. These are often referred to as "curvature terms". These are usually small in astrophysical applications, as $\frac{1}{\sqrt{\mu\rho_0}}B_\phi/s$ is negligible compared to $s\mathrm{d}_s\Omega_K$ (where Ω_K is the Keplerian angular velocity). In the present study, devoted to planetary interiors, however, one needs to compare the squared relative differential rotation $(\Delta\Omega/\Omega)^2$ with $\beta^2 E\Lambda/Pm$. Some assumption is needed both on $\Delta\Omega$ and on β for which we lack direct measurements, however both terms are of the same order of magnitude for a wide range of sensible values.

Using the WKB approach, perturbations take the form $\exp(\sigma t + i(k_s s + k_z z))$ where σ is the growth rate, k_s and k_z are respectively the radial and the axial wavenumbers. We introduce the notation $V_{Az} = B_z/\sqrt{\mu\rho_0}$ $V_{A\phi} = B_\phi/\sqrt{\mu\rho_0}$, and note $\omega_z = k_z V_{Az}$ and $\omega_\eta = \eta k^2$ with $k^2 = k_s^2 + k_z^2$.

The second order dispersion relation then takes the form

$$\mathcal{A}\sigma^2 + \mathcal{B}\sigma + \mathcal{C} = 0, \tag{11}$$

with

$$\mathcal{A} = 4\Omega^2, \qquad \mathcal{B} = 8\Omega^2\omega_\eta - 2\Omega 8i\frac{V_{A\phi}}{s}\omega_z, \tag{12}$$

and

$$\mathcal{C} = -\omega_z^2 s\frac{\mathrm{d}}{\mathrm{d}s}\left(\frac{V_{A\phi}^2}{s^2}\right) - 4\omega_z^2\frac{V_{A\phi}^2}{s^2} + \frac{k^2}{k_z^2}\omega_z^4 + 2\Omega s\frac{\mathrm{d}\Omega}{\mathrm{d}s}\omega_z^2 + 4\Omega^2\omega_z^2 + 8\Omega\omega_\eta i\frac{V_{A\phi}}{s}\omega_z. \quad (13)$$

The solution takes the form

$$\sigma = -\frac{\mathcal{B}}{2\mathcal{A}} + \sqrt{\omega_z^2\left(s\frac{\mathrm{d}}{\mathrm{d}s}\left(\frac{V_{A\phi}^2}{s^2}\right) - 2\Omega s\frac{\mathrm{d}\Omega}{\mathrm{d}s}\right) - \frac{k^2}{k_z^2}\omega_z^4}. \quad (14)$$

Eq. (14) reveals, as noted by Acheson and Hide (1973) for non-axisymmetric disturbances, that a positive gradient of B_ϕ/s has the same destabilizing action as an outwardly decreasing angular velocity. Fearn (1993) considered a very similar stability criterion with an azimuthal field only (see his Eq. (3)). In the presence of a purely toroidal field, axisymmetric disturbances are strongly stabilized by the rapid global rotation. An applied axial field allows the development of an axisymmetric instability. The analogy between B_ϕ/s and Ω also holds for axisymmetric disturbances in the presence of an helical field.

As in Petitdemange et al. (2008), the most unstable mode corresponds to $k_s = 0$. The growth rate is a decreasing function of k_s. In order to satisfy the local assumption necessary for a WKB analysis, we therefore need to consider unstable modes in the limit $k_s \ll k_z$.

It is interesting to note that $\mathcal{B}$ does not depend on the derivatives of B_ϕ and Ω. $\mathcal{B}$ has a non-vanishing imaginary part for $B_\phi \neq 0$. Unstable perturbations therefore grow exponentially with the phase velocity

$$c_z = -\frac{V_{A\phi}}{s}\frac{V_{Az}}{\Omega}. \quad (15)$$

Since the imaginary part of the growth rate depends linearly on k_z, the group velocity is here equal to the phase velocity, the wave packet is not modified as the instability proceeds along the z-direction.

As noted above c_z does not directly depend on the shear rate $\mathrm{d}\Omega/\mathrm{d}s$. It should however be noted that the magnitude of the shear rate obviously controls that of the background field B_ϕ through the ω-effect (e.g. Dormy and Soward, 2007).

In order to get a crude estimate of the order of magnitude of c_z, we approximate s by the unit of length and divide the phase/group velocity by $L\Omega$ to make it non-dimensional

$$\frac{c_z}{L\Omega} = \frac{\beta E\Lambda}{Pm} = Q. \quad (16)$$

Because of the smallness of the Ekman number in planetary interiors ($E \sim 10^{-15}$ for the Earth's outer core), the drift time appears long compared with the short growth time. We may therefore argue that, in the magnetostrophic regime, axisymmetric perturbations are only slightly modified by a background toroidal magnetic field. The drift will be slow and the growth rate is unaffected by a $B_\phi \propto s$.

Following the same approach as Petitdemange et al. (2008), we identify the axial wavenumber k_{zmax} for which $\sigma = \sigma_{max}$ (maximum growth rate). We identify k_{zmax} by solving $\mathrm{dIRe}(\sigma)/\mathrm{d}k_z = 0$. The following equation results

$$4\left(s\frac{\mathrm{d}}{\mathrm{d}s}\left(\frac{V_{A\phi}^2}{s^2}\right) - \omega_{zmax}^2 + 4\Omega^2 Ro'\right)\frac{\omega_{zmax}^2}{\Lambda^2} = \left(4\Omega^2 Ro' + s\frac{\mathrm{d}}{\mathrm{d}s}\left(\frac{V_{A\phi}^2}{s^2}\right) - 2\omega_{zmax}^2\right)^2, \quad (17)$$

which can be rewritten as a polynomial equation for ω_{zmax}^2

$$\omega_{zmax}^4 - \left[4\Omega^2 Ro' + s\frac{\mathrm{d}}{\mathrm{d}s}\left(\frac{V_{A\phi}^2}{s^2}\right)\right]\omega_{zmax}^2 + \frac{\left(4\Omega^2 Ro' + s\frac{\mathrm{d}}{\mathrm{d}s}\left(\frac{V_{A\phi}^2}{s^2}\right)\right)^2}{4(1+\Lambda^{-2})} = 0, \quad (18)$$

where we have introduced the shear rate $Ro' = (s/2\Omega)\mathrm{d}\Omega/\mathrm{d}s$. The physically meaningful wave number solution is then

$$\omega_{zmax}^2 = k_{zmax}^2 V_{Az}^2 = \left(2\Omega^2 Ro' + \frac{1}{2}\frac{\mathrm{d}}{\mathrm{d}s}\left(\frac{V_{A\phi}^2}{s^2}\right)\right)\left(1 - (1+\Lambda^{-2})^{-1/2}\right). \quad (19)$$

If we now adopt an observational point of view, the axial drift can only be identified over a typical distance $\lambda_z = 2\pi/k_z$. Using k_{zmax} and Eq. (16), the characteristic timescale for axial drift can then be estimated

$$\Omega\tau_{c_z} = \frac{2\pi}{\beta}\sqrt{\frac{Pm}{2E\Lambda|Ro'|\left(1-(1+\Lambda^{-2})^{-1/2}\right)}}, \quad (20)$$

where we assumed $B_\phi \propto s$. An estimate of this timescale for the Earth interior would be as short as the amplification time of the most rapidly growing MS-MRI mode (see Petitdemange et al., 2008; Soward and Jones, 1983), i.e. of the order of a year, either if the condition $\beta > 3000$ is realized, or if the instability takes place close to the axis of rotation (where the effects of curvature are stronger).

Inserting k_{zmax} in Eq. (14) provides the maximum growth rate

$$\mathrm{IRe}(\sigma_{max}) = \left[s\left|\frac{\mathrm{d}\Omega}{\mathrm{d}s}\right| + \frac{1}{2\Omega}s\frac{\mathrm{d}}{\mathrm{d}s}\left(\frac{V_{A\phi}^2}{s^2}\right)\right]\frac{\Lambda/2}{1+\sqrt{1+\Lambda^2}}, \quad (21)$$

which can be compared with Petitdemange et al. (2008) Eq. (25). The growth rate is unaffected by a background field proportional to s. This is consistent with the numerical results presented above, in which $\mathrm{IRe}(\sigma)$ does not depend on β (see Table 1).

In order to understand how the magnitude of β affects the ratio R_E of the magnetic energy to the kinetic energy, we sum the squares of the Eqs. (7) and (8) and using the WKB approximation, we obtain

$$4\Omega^2(u_s^2+u_\phi^2) = \left(-\omega_z^2 + 4\frac{V_{A\phi}^2}{s^2}\right)(b_s^2+b_\phi^2) + \left(s\frac{\mathrm{d}}{\mathrm{d}s}\left(\frac{V_{A\phi}}{s}\right)b_s\right)^2 + 2b_s s\frac{\mathrm{d}}{\mathrm{d}s}\left(\frac{V_{A\phi}}{s}\right)\left(i\omega_z b_\phi + 2\frac{V_{A\phi}}{s}b_s\right). \quad (22)$$

Obviously R_E takes a very simple form if $V_{A\phi} \propto s$. We note that if $\beta Q \ll 1$, R_E will be large compared to unity (as expected in the magnetostrophic regime). However, in the parameter regime which can be addressed numerically, this condition is not met, and R_E is therefore affected by β as shown in Table 1.

In addition, our choice for the B_ϕ dependency maximizes R_E. In realistic numerical models, such as self excited dynamos, the realized B_ϕ could be much more complicated. However, in the magnetostrophic limit $\beta Q \ll 1$, correction terms in (22) would be small and even sharp variation of B_ϕ would therefore not prevent $R_E \gg 1$.

In order to identify the MS-MRI mode, it is essential to determine how the background toroidal field can affect the relationship between b_s, b_ϕ and u_s. At first, from the radial component of the induction equation, the relation between u_s and b_s is deduced. This equation is similar to the one derived in Petitdemange et al. (2008). However, since the growth rate possesses an imaginary part which depends on Q, the phase shift is not any more fixed for moderate

Ekman numbers. Relying on the magnetostrophic balance to eliminate velocity perturbations in the induction equation, we obtain (with $k_s = 0$ for simplicity)

$$\left(\sigma + \eta k_z^2 - \frac{i\omega_z}{\Omega}\frac{V_{A\phi}}{s}\right) b_\phi = \left(\frac{\omega_z^2}{2\Omega} + s\frac{\mathrm{d}\Omega}{\mathrm{d}s} - s\frac{\mathrm{d}}{\mathrm{d}s}\left(\frac{V_{A\phi}}{s}\right)\right) b_s, \tag{23}$$

$$\left(\sigma + \eta k_z^2 - \frac{i\omega_z}{2\Omega s}\frac{\mathrm{d}(sV_{A\phi})}{\mathrm{d}s}\right) b_s = -\frac{\omega_z^2}{2\Omega} b_\phi. \tag{24}$$

The phase shift between b_s and b_ϕ appears clearly in replacing σ by σ_{max}. We note

$$\mathrm{IIm}(\sigma) - \frac{\omega_z}{2\Omega s}\partial_s(sV_{A\phi}) = -\frac{\omega_z}{2\Omega}\frac{\mathrm{d}}{\mathrm{d}s}\left(\frac{V_{A\phi}}{s}\right). \tag{25}$$

The phase shift depends on the derivative $\mathrm{d}(B_\phi/s)/\mathrm{d}s$. The configuration $B_\phi \propto s$ yields a b_s half of a period out of phase with b_ϕ, as shown in Fig. 1.

The classical MS-MRI mechanism is modified by the helical structure of the background field. The modified phase shift and the group/phase velocity tend to disappear in the magnetostrophic limit for axisymmetric modes. As a result, the MS-MRI mode as presented in Petitdemange et al. (2008) would be unaffected by a smooth background toroidal field in the limit relevant to planetary interiors. However, this additional component complicates the identification of the MS-MRI in DNS, as it modifies the phase relationship between u_s, b_s and b_ϕ and the ratio R_E.

The simple WKB approximation used above relies on several simplifying assumptions which are not always realized in practice. We use this here as a first step toward understanding the basic underlying phenomena observed in our DNS (which is of course free of such assumptions). The description provided by the WKB approach, while simple, provides a surprisingly accurate interpretation of our numerical results.

4. Non-axisymmetric MS-MRI

We now want to investigate non-axisymmetric MS-MRI modes arising from the same background state. In the astrophysical context, Balbus & Hawley (1992 paper IV) performed a local stability analysis for 3D MRI modes using shearing coordinates. Since the authors were interested in weakly magnetized accretion disks, they did not take into account the curvature terms associated with the background magnetic field. For strongly magnetized astrophysical plasmas, Pessah and Psaltis (2005) have shown that the curvature terms associated with the toroidal field lines can play an important role in strongly magnetized accretion disks. Let us recall that, in planetary interiors, *curvature terms* cannot be neglected.

We begin with a description ignoring background magnetic gradients. In order to highlight the effects of magnetic curvature terms, we first perform a simple WKB analysis using shearing planar coordinates. Whereas for the MRI, the axisymmetric mode is always the most unstable, for more arbitrary magnetic configurations, non-axisymmetric modes can at least be transiently more important, but these ultimately die away as the wavenumber becomes strongly sheared (see Soward and Jones, 1983). We then investigate the effect of the magnetic curvature terms.

4.1. Local analysis in shearing cartesian coordinates

In a shearing coordinates, the radial wavenumber becomes time dependent according to

$$k_s(t) = k_s(0) - m\frac{\mathrm{d}\Omega}{\mathrm{d}s}t. \tag{26}$$

If the background magnetic field involves a radial component, the azimuthal field will grow linearly with time

$$B_\phi(t) = B_\phi(0)\left(1 + \frac{B_s}{B_\phi(0)}s\frac{\mathrm{d}\Omega}{\mathrm{d}s}\right), \tag{27}$$

where $B_\phi(0)$ is the initial toroidal field. From the last two equations, we deduce that $\mathbf{k}\cdot\mathbf{B}$ does not depend on time. The perturbed linearized MHD equations in the magnetostrophic regime are then

$$k_s u_s + \frac{m}{s}u_\phi + k_z u_z = 0, \tag{28}$$

$$-2\Omega u_\phi + \frac{ik_s}{\mu\rho}(p' + \mathbf{B}\cdot\mathbf{b}) - i\frac{\mathbf{k}\cdot\mathbf{B}}{\mu\rho}b_s = 0, \tag{29}$$

$$2\Omega u_s + \frac{im}{s\mu\rho}(p' + \mathbf{B}\cdot\mathbf{b}) - i\frac{\mathbf{k}\cdot\mathbf{B}}{\mu\rho}b_\phi = 0, \tag{30}$$

$$k_z(p' + \mathbf{B}\cdot\mathbf{b}) - \mathbf{k}\cdot\mathbf{B}b_z = 0, \tag{31}$$

$$\frac{\mathrm{d}b_s}{\mathrm{d}t} + \eta k_{tot}^2 b_s = i\mathbf{k}\cdot\mathbf{B}u_s, \tag{32}$$

$$\frac{\mathrm{d}b_\phi}{\mathrm{d}t} + \eta k_{tot}^2 b_\phi = s\frac{\mathrm{d}\Omega}{\mathrm{d}s}b_s + i\mathbf{k}\cdot\mathbf{B}u_\phi, \tag{33}$$

$$\frac{\mathrm{d}b_z}{\mathrm{d}t} + \eta k_{tot}^2 b_z = i\mathbf{k}\cdot\mathbf{B}u_z, \tag{34}$$

where $\mathrm{d}/\mathrm{d}t$ denotes Lagrangian time derivative, $k_{tot}^2 = k_s^2 + m^2/s^2 + k_z^2$, and $p' = p\mu$. We combine these equations in order to eliminate the perturbed pressure term p' in the equation of motion

$$-2\Omega u_\phi + \frac{ik_s}{k_z\mu\rho}\mathbf{k}\cdot\mathbf{B}b_z - i\frac{\mathbf{k}\cdot\mathbf{B}}{\mu\rho}b_s = 0. \tag{35}$$

From $\nabla\cdot\mathbf{b} = 0$, we get $b_z = -(mb_\phi/s + k_s b_s)/k_z$. As a result, Eq. (35) becomes

$$2\Omega u_\phi + i\frac{\mathbf{k}\cdot\mathbf{B}}{\mu\rho}\left(\frac{k_{sz}^2}{k_z^2}b_s + \frac{mk_s}{sk_z}b_\phi\right) = 0, \tag{36}$$

and the azimuthal component is

$$2\Omega u_s = \frac{imk_s}{sk_z^2}\mathbf{k}\cdot\mathbf{V_A}b_s + i\frac{k_{zm}^2}{k_z^2}\mathbf{k}\cdot\mathbf{V_A}b_\phi. \tag{37}$$

We have introduced the following notations

$$k_{zm}^2 = k_z^2 + m^2/s^2, \qquad k_{zs}^2 = k_z^2 + k_s^2, \qquad k_{tot}^2 = k_s^2 + k_z^2 + m^2/s^2. \tag{38}$$

Using (36) and (37), we substitute u_s and u_ϕ in the induction equation

$$\frac{\mathrm{d}b_\phi}{\mathrm{d}t} + \eta k_{tot}^2 b_\phi = \frac{(\mathbf{k}\cdot\mathbf{B})^2}{2\Omega\mu\rho}\left(\frac{k_{sz}^2}{k_z^2}b_s + \frac{mk_s}{sk_z^2}b_\phi\right) + s\frac{\mathrm{d}\Omega}{\mathrm{d}s}b_s, \tag{39}$$

$$\frac{\mathrm{d}b_s}{\mathrm{d}t} + \eta k_{tot}^2 b_s = -\frac{(\mathbf{k}\cdot\mathbf{B})^2}{2\Omega\mu\rho}\left(\frac{mk_s}{sk_z^2}b_s + \frac{k_z^2 + m^2/s^2}{k_z^2}b_\phi\right). \tag{40}$$

Let us rewrite this system in the form of a single ODE, differentiating (40) with time we write

$$\frac{\mathrm{d}b_\phi}{\mathrm{d}t} = -\frac{mk_s}{sk_{zm}^2}\frac{\mathrm{d}b_s}{\mathrm{d}t} + \frac{m^2}{sk_{zm}^2}\frac{\mathrm{d}\Omega}{\mathrm{d}s}b_s \tag{41}$$

$$-\frac{2\Omega}{(\mathbf{k}\cdot\mathbf{V_A})^2}\frac{k_z^2}{k_{zm}^2}\left(\eta k_{tot}^2\frac{\mathrm{d}b_s}{\mathrm{d}t} + \frac{\mathrm{d}^2 b_s}{\mathrm{d}t^2} - 2\eta k_s m\frac{\mathrm{d}\Omega}{\mathrm{d}s}b_s\right). \tag{42}$$

Substitution in (39) yields

$$\frac{d^2 b_s}{dt^2} + \frac{s}{2\Omega}\frac{d\Omega}{ds}(\mathbf{k}\cdot\mathbf{V_A})^2 b_s + \frac{(\mathbf{k}\cdot\mathbf{V_A})^4}{4\Omega^2}\frac{k_{tot}^2}{k_z^2} b_s + 2\eta k_{tot}^2 \frac{db_s}{dt} - 2\eta k_s \frac{m}{s} s\Omega' b_s + \eta^2 k_{tot}^4 b_s = 0. \quad (43)$$

The coefficients of this simple second order ODE are time dependent through k_s. This wavenumber grows linearly with time and either diffusion or magnetic tension act to stabilize the resulting small scale structures. As a result, non-axisymmetric modes appear as transient events (Balbus and Hawley, 1992; Terquem and Papaloizou, 1996). Indeed, even without diffusion, the increase of k_s with time enhances the stabilizing effect of the magnetic tension term $k_{tot}^2(\mathbf{k}\cdot\mathbf{V_A})^4/k_z^2$. Non-axisymmetric modes are amplified only until the magnetic tension term exceeds the destabilizing term (which is not time dependent).

Fig. 3 exhibits solutions for different azimuthal wave numbers m, a purely axial background field, and parameters relevant to planetary interiors: $E = 10^{-15}, Pm = 10^{-5}$, $\Lambda = 1$ and $Ro' = s/2d(\ln\Omega)/ds = 3.10^{-4}$. We consider an axial wavenumber $k_z L = 100$, where L is the unit of length. Whereas for the classical MRI, the axisymmetric mode is by far the most unstable one, in rapidly rotating systems, the growth rates for small m are close to that of $m = 0$ even for a purely axial background field. The transient amplification, occurring while $k_s(t) \leqslant k_z$, is significant for low values of m.

Let us now consider the effect of a background toroidal field B_ϕ. This component is potentially important because a non-vanishing toroidal field introduces a dependence of $\mathbf{k}\cdot\mathbf{V_A}$ on m. In contrast, a radial component B_s in the applied field would not introduce such a dependence. There is therefore no loss of generality in assuming $B_s \equiv 0$, as $\mathbf{k}\cdot\mathbf{B}$ is unaffected in 26,27 (see Balbus and Hawley, 1992, paper IV).

Fig. 4 shows solutions obtained for $k_z L = 20$ and $B_\phi/B_0 = 100$ and $B_\phi/B_0 = 300$. For the largest magnitude of B_ϕ, stabilization from magnetic tension exceeds that from resistivity. As a result, the most unstable mode is associated with the smallest magnetic tension, i.e. $m = 1$. Decreasing B_ϕ allows the dominance of larger m modes. But in all cases, the amplification is only transient.

Let us turn to the more general case in which both B_ϕ and B_z are on an equal footing. According to previous results, it is not surprising that using a helical background field amplifies axisymmetric and non-axisymmetric modes (see Fig. 5). The magnitude of B_ϕ determines which mode is the most amplified.

In the parameter regime currently accessible by DNS, transient amplification of non-axisymmetric modes will also be observed

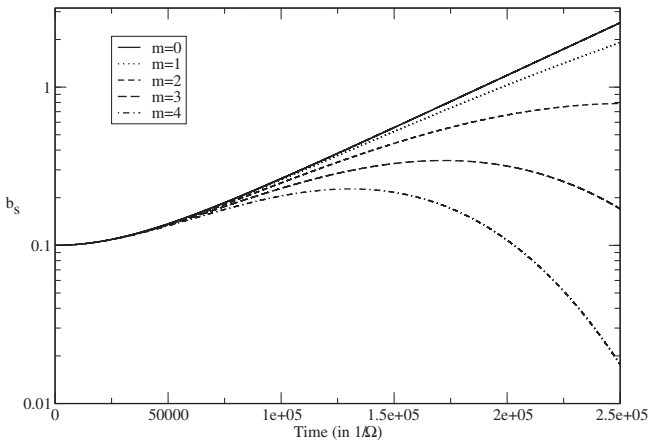

Fig. 3. Non-axisymmetric solutions with a purely axial background field. Small m modes initially grow, with the same rate as the axisymmetric mode, until damped by phase mixing. Non-axisymmetric events are transient processes with a significant amplification for small values of m.

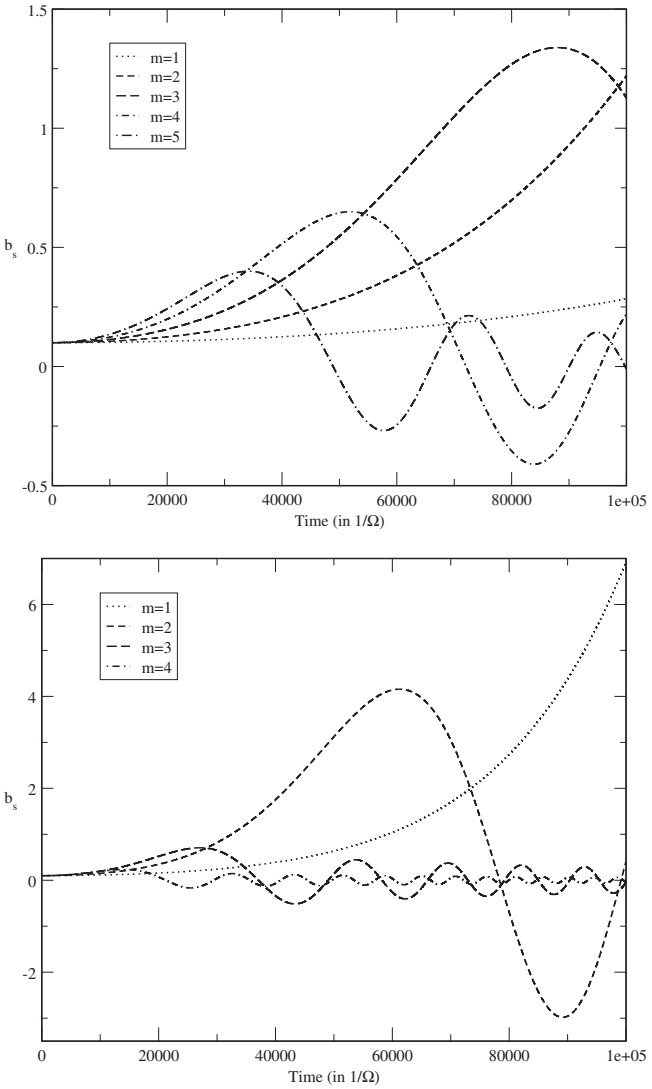

Fig. 4. Non-axisymmetric solutions obtained considering a purely toroidal background field with magnitudes $B_\phi/B_0 = 100$ (top) and $B_\phi/B_0 = 300$ (bottom), with $k_z L = 20$ in order to limit resistive effects. All other dimensionless parameters are identical to Fig. 3.

when β and Λ exceed unity, as illustrated on Fig. 6. This shows that non-axisymmetric modes can play an important role in DNS and numerical dynamos.

4.2. Local analysis with curvature terms using shearing coordinates

The non-axisymmetric local analysis performed above does not take into account curvature terms associated with the background toroidal magnetic field. Since a radial component of the background field yields a time dependent toroidal field, we treat here only a helical background field, without a radial component.

The derivation is essentially similar to the previous section, but including field curvature terms; details may be found in the appendix. Assuming $B_\phi \propto s$, the resulting ODE is

$$\frac{d^2 b_s}{dt^2} + \left(2\Omega\eta k_{tot}^2 - 2Fi\mathbf{k}\cdot\mathbf{V_A}\right)\frac{db_s}{dt} + \left(\eta k_{tot}^2 - \frac{Fi\mathbf{k}\cdot\mathbf{V_A}}{\Omega}\right)^2 b_s + \frac{k_{tot}^2}{k_z^2}\frac{(\mathbf{k}\cdot\mathbf{V_A})^4}{4\Omega^2} b_s + (\mathbf{k}\cdot\mathbf{V_A})^2 \frac{s\Omega'}{2\Omega} b_s - 2\eta s\Omega' \frac{mk_s}{s} b_s = 0, \quad (44)$$

where $F = V_{A\phi}/s$.

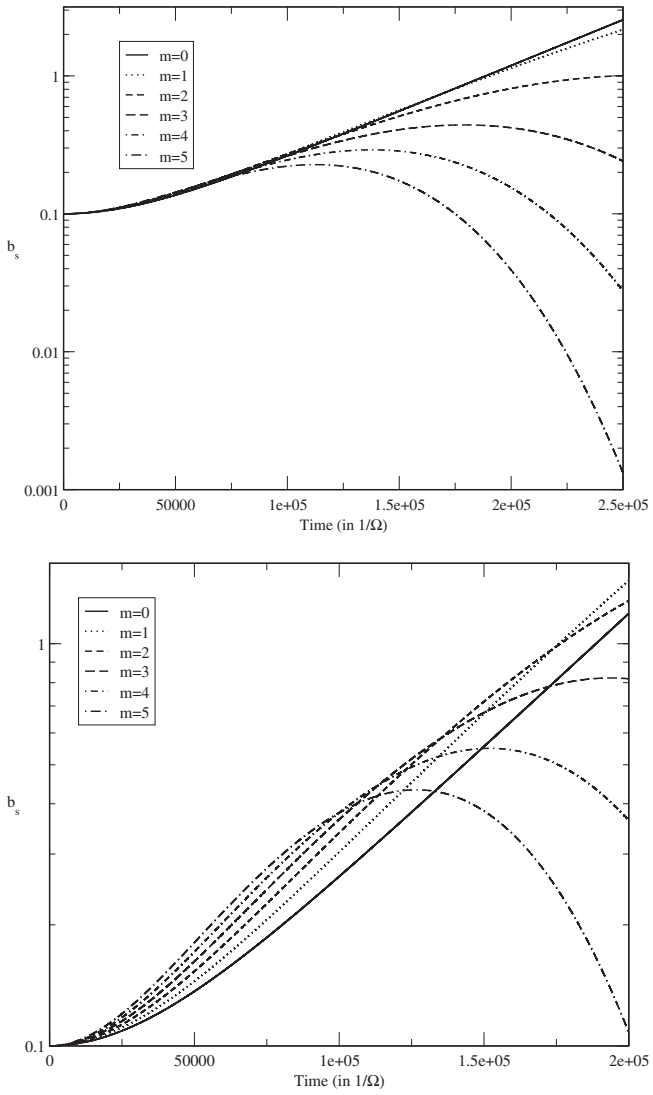

Fig. 5. Solutions obtained for a background helical field using cartesian shearing coordinates with $k_zL = 100$ and $B_\phi = 3B_z$ (top) and $B_\phi = 10B_z$ (bottom).

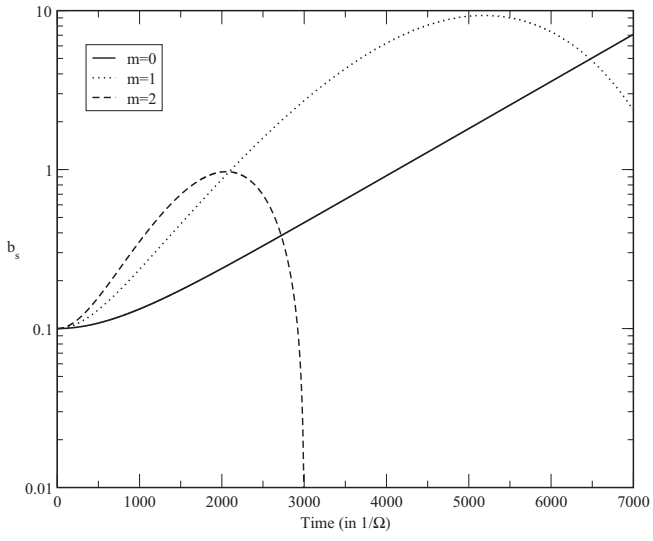

Fig. 6. Solutions obtained for a background helical field with $B_\phi = 20B_z$ and $k_zL = 20$ using cartesian shearing coordinates. The parameters are $E = 10^{-7}$, $\Lambda = 2, Pm = 0.5$ and $Ro' = 0.0045 \simeq E^{1/3}$.

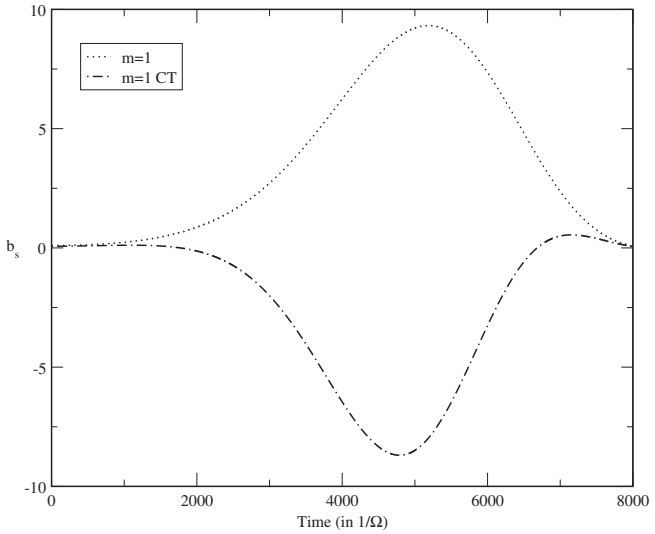

Fig. 7. Action of curvature terms on the transient amplification of the $m = 1$ mode. The parameters are the same as in Fig. 6, the initial value of b_s is here set to 0.1.

Curvature terms introduce out-of-phase imaginary coefficients. For the non-axisymmetric modes, these terms yield oscillatory, but transient, behavior. For the values of B_ϕ considered, the real part of the eigenvalue (the growthrate) is unaffected by curvature terms.

On the other hand, for a numerically tractable parameter regimes, the imaginary part can be significant. For instance, on Fig. 7, the solution is strongly modified by the action of curvature terms. The amplification remains significant. Transient events can still be strongly amplified and can dominate the axisymmetric mode for an appreciable period of time.

4.3. Linear direct numerical simulations

We consider the same background state as introduced in Section 2.1 and the same linearized MHD equations, but the perturbed quantities $(\mathbf{u}, \mathbf{b})$ are now three-dimensional. Our numerical results are summarized in Tables 2 and 3.

We can interpret our numerical results in the light of the above local description. Let us stress however that in the full numerics, we consider weak background shear rates. The relation $k_zL > m$ is always met, but the approximation $k_zL \gg m$, used in the analytical description, is not justified for such parameters.

First, it should be stressed that in the local approach with phase mixing, we obtain only transient amplification of the non-axisymmetric modes. DNS seem to show that these modes can be destabilized at larger forcing parameters. Such a situation (linear instability at larger forcing to counteract phase mixing) can be tackled analytically (see for example Soward and Jones, 1983; Jones et al., 2000). We do not attempt such a study here, but the numerics is performed in a regime in which non-axisymmetric modes can grow while preventing lengthscale shortening. Non-axisymmetric exponentially growing modes have also been obtained by Kitchatinov and Rüdiger (2010) for MRI modes in Keplerian accretion disks model.

The structure of the helicoidal eigenmode, which is well described in the local limit, is shown in Fig. 8. The presence of the toroidal field significantly modifies the phase relation between b_s, b_ϕ and u_s for non-axisymmetric modes. We have observed for such modes a pattern similar to that of Fig. 1. The kinetic energy is azimuthally and axially shifted by half of period compared with the magnetic one. Non-axisymmetric modes have a particular helical structure which clearly appears as the magnetostrophic regime

Table 2
Numerical results for 3D perturbed variables. The growth rates ($\times 10^2$) are given for different azimuthal wave numbers m and dimensionless parameters.

Ro	β	m=0	m=1	m=2	m=3	m=4	m=5	m=6
$2E = 2.10^{-5}$, $Pm = 0.5$, $2\Lambda = 2$								
0.03	10	2.64	5.55	5.02	1.93			
$2E = 10^{-5}$, $Pm = 0.5$, $2\Lambda = 2$								
0.03	0	3.9	3.30	1.13				
	1	3.9	3.75	2.36	0.51			
0.03	10	3.84	6.75	4.57	4.73	2.77		
0.01	10	0.99	1.79	1.24	0.93			
0.01	3	0.96	1.23	1.16	0.48			
$2E = 10^{-5}$, $Pm = 0.5$, $2\Lambda = 1$								
0.01	3	0.46	0.59	0.27				
$2E = 10^{-5}$, $Pm = 0.5$, $2\Lambda = 0.5$								
0.01	10	0.033	0.18	0.51	0.33			
$2E = 10^{-5}$, $Pm = 0.5$, $2\Lambda = 0.25$								
0.01	10	0.035	0.21	0.34	0.41	0.25		
$2E = 5.10^{-6}$, $Pm = 0.5$, $2\Lambda = 2$								
0.03	0	1.89	1.6	0.65				
0.005	0	0.48	0.36					
$2E = 3.10^{-6}$, $Pm = 0.5$, $2\Lambda = 2$								
0.03	0	3.41	3.39	2.51	0.81			
0.01	10	1.28	1.88	2.03	1.19	0.86	0.60	
	3	1.28	1.32	1.00	0.59	0.37	0.24	0.1
	1	1.26	1.06	0.53				
0.01	0	1.24	1.03					
$2E = 3.10^{-6}$, $Pm = 0.25$, $2\Lambda = 2$								
0.01	3	1.12	1.29	1.13	0.73	0.42	0.18	

Table 3
The values of the R_E ratio (ratio of the magnetic over kinetic energy) for the numerical simulations listed in Table 2.

Ro	β	m= 0	m=1	m=2	m=3	m=4	m=5	m=6
$2E = 2.10^{-5}$, $Pm = 0.5$, $2\Lambda = 2$								
0.03	10	11	8.5	8.3	7.7			
$2E = 10^{-5}$, $Pm = 0.5$, $2\Lambda = 2$								
0.03	0	47.9	38.91	25.2	5.5			
	1	47.5	37.1	23.7	9.8			
0.03	10	20.2	14	9.8	9.1	8.5		
0.01	10	45.5	27.5	24.5	23			
0.01	3	110	82.1	48.5	23.2			
$2E = 10^{-5}$, $Pm = 0.5$, $2\Lambda = 1$								
0.01	3	217.5	132.5	73.9				
$2E = 10^{-5}$, $Pm = 0.5$, $2\Lambda = 0.5$								
0.01	10	261	98.5	40.7	31			
$2E = 10^{-5}$, $Pm = 0.5$, $2\Lambda = 0.25$								
0.01	10	309.8	117	38	30.4	22.6		
$2E = 5.10^{-6}$, $Pm = 0.5$, $2\Lambda = 2$								
0.03	0	98.1	79	52.6				
0.005	0	293	244					
$2E = 3.10^{-6}$, $Pm = 0.5$ $2\Lambda = 2$								
0.03	0	40	39	31				
0.01	10	95	60	37	27	24.5	24	
	3	151	105	66	47	23	16	11
	1	158	123	81				
0.01	0	155	121					
$2E = 3.10^{-6}$, $Pm = 0.25$, $2\Lambda = 2$								
0.01	3	137	95	58	39	23	14	

is approached. The phase shift between the components is then identical to that described in Petitdemange et al. (2008).

The ratios given in Table 3 provide information on the possibility to try to observe the signature of this instability in geomagnetic measurements or in dynamo models. In Petitdemange (2010), the saturation process of the axisymmetric MS-MRI has been highlighted. As R_E is very large for axisymmetric modes, the magnitude of the induced magnetic field significantly exceeds that of the induced velocity field. It was shown that such a magnetic field induces a nonlinear geostrophic flow, which rapidly becomes the dominant one. Since the MS-MRI fingerprint lies in the relationship between the magnetic and velocity fields, this non-linear geostrophic flow complicates the possible identification of the modes in observations or in direct numerical simulations of the geodynamo.

According to the values of R_E reported in Table 3, non-axisymmetric modes would be more easily detectable in direct numerical simulations, even if these modes drift axially. In the magnetostrophic regime, $R_E \gg 1$ because of the smallness of the Ekman number. Even if $\beta = 0$, the ratio R_E is a decreasing function of m.

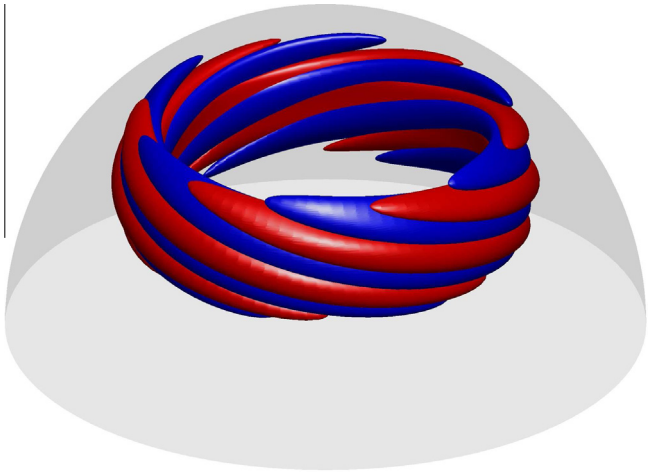

Fig. 8. Isosurfaces of the magnetic energy in red (10% of the maximum value) and of the kinetic energy in blue (40% of the maximum value), for an unstable $m = 3$ mode and with $2E = 3 \cdot 10^{-6}$, $Pm = 0.5$, $\Lambda = 1$, and $Ro = 10^{-2}$. (For interpretation of the references to colour in this figure legend, the reader is referred to the web version of this article.)

5. Non-linear saturation

In the previous section, we have discussed the MS-MRI saturation mechanism, which has been determined from axisymmetric direct numerical simulations in Petitdemange (2010). Here, we investigate the effect induced by an additional toroidal background field. We now consider a non-linear version of equations (1) and (2)

$$\frac{\partial \mathbf{u}}{\partial t} + [(\mathbf{U_0} + \mathbf{u}) \cdot \nabla](\mathbf{U_0} + \mathbf{u}) = -2\mathbf{e_z} \times \mathbf{u} + E\Delta\mathbf{u} - \nabla\pi + \frac{\Lambda E}{Pm}[(\nabla \times (\mathbf{B_0} + \mathbf{b})) \times (\mathbf{B_0} + \mathbf{b})], \tag{45}$$

$$\frac{\partial \mathbf{b}}{\partial t} = \frac{E}{Pm}\Delta\mathbf{b} + \nabla \times [(\mathbf{U_0} + \mathbf{u}) \times (\mathbf{B_0} + \mathbf{b})]. \tag{46}$$

5.1. Axisymmetric non-linear simulations

Fig. 9 shows that the axial drift velocity is unaffected by the saturation process. This also occurred in the local description, for which the group/phase velocity does not depend on the background shear rate. The non-linearly induced geostrophic flow modifies the background velocity field and allows the saturation of the

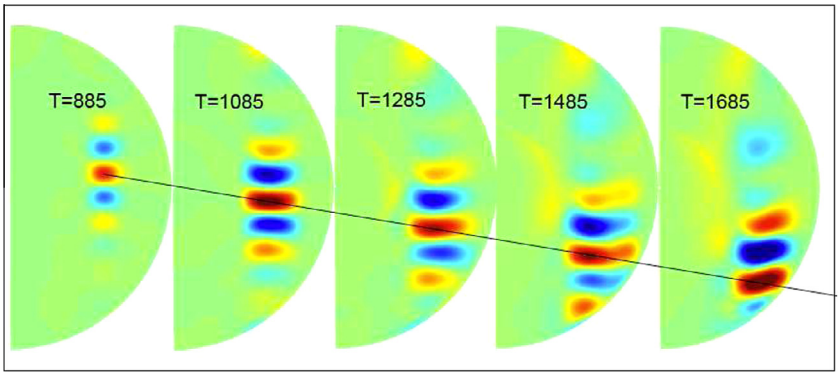

Fig. 9. Meridional sections showing the temporal evolution of the induced toroidal magnetic field. The radial expansion evolves with time, indicating that saturation is taking place. This process occurs while maintaining a constant drift velocity. This non-linear simulation was performed with parameters $2E = 10^{-5}, \Lambda = 1, Pm = 0.5, Ro = 0.01$ and $\beta = 10$.

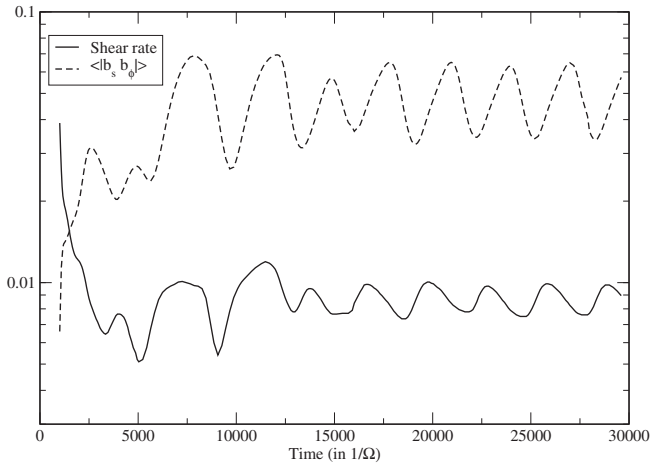

Fig. 10. Time evolution of the maximum shear rate (lower curve) and $\langle |b_s b_\phi| \rangle$ (upper curve), where $\langle \cdot \rangle$ denotes the mean value over the whole numerical domain. Dimensionless parameters for this simulation are $2E = 10^{-5}, Pm = 0.5, \Lambda = 1, Ro = 0.01$ and $\beta = 3$.

instability, yet the structures continue to propagate until they reach the boundary of the numerical domain.

When the structures reach the boundary of the domain, they vanish in boundary layers. As a result, the absolute value of the product $-b_s b_\phi$ averaged on the whole numerical domain (hereafter denoted by $-\langle b_s b_\phi \rangle$) evolves with time (see Fig. 10). Let us recall that this quantity is responsible for the non-linear geostrophic flow which compensates the background velocity field through a reduction of the shear. Decreasing $\langle |b_s b_\phi| \rangle$ affects the magnitude of the nonlinear flow and $\mathbf{U_0} + \mathbf{u}$ appears with a sharper profile. But, increasing the shear rate destabilizes MS-MRI modes which amplify again $\langle b_s b_\phi \rangle$ and the differential rotation is reduced, this mechanism takes the form of a relaxation oscillation. Fig. 10 shows numerical results illustrating this behavior. The maximum shear rate is the maximum of $\mathrm{d}(\mathbf{U_0} + \mathbf{u})/s)/\mathrm{d}s$ computed over the fluid domain.

5.2. Three-dimensional non-linear simulations

Direct three-dimensional (3D) simulations with low Ekman numbers require significant numerical resources, so we have used only 30 azimuthal Fourier modes. The simulations performed are listed in Table 4. We have limited the time integration to the beginning of the saturation process, and interrupted the simulations when the maximum shear rate had decreased by a factor of eight. We therefore do not expect to observe the relaxation oscillations described in Fig. 10.

Table 4
List of performed 3D simulations. The Ekman number is set to $2E = 10^{-5}$ in all cases. In order to achieve such parameters, we consider only $0 \leqslant m \leqslant 30$ azimuthal modes, whereas the number of spherical harmonics is $l_{max} = 250$ and the domain is radially discretized using 352 points.

Run	Λ	Pm	Ro	β
R1	1	0.5	0.03	0
R2	1	0.5	0.03	1
R3	2	0.5	0.01	3
R4	2	0.5	0.01	10
R5	2	0.5	0.03	20

As simulations with small magnetic Prandtl numbers are numerically very demanding, we use $Pm = \nu/\eta = 0.5$. Smaller values are unfortunately computationally out of reach with present computers. Since we are interested in the magnetostrophic regime, we choose $\Lambda = 1$. We have also performed simulations with $\Lambda = 2$, and observed an increase of the axial drift rate.

We want to investigate the onset of the nonlinear behavior. As expected from the linear description, the results obtained from runs denoted R1 and R2 indicate that transient amplification plays a minor role when the background toroidal field is weak. Saturation occurs by a reduction of the shear, as previously reported for axisymmetric configurations (see Petitdemange, 2010).

An interesting and unexpected feature appears when Q is increased. Fig. 11 shows the persistence of non-axisymmetric events for a longer time than predicted by linear theory. Indeed, the $m = 1$ mode is still dominant at the end of both simulations R3 and R5. Saturation is still caused by the modification of the total flow ($\mathbf{U_0} + \mathbf{u}$). A non-linear axisymmetric geostrophic flow was induced by the Maxwell stress (as discussed in Petitdemange, 2010). This results in a flattened and radially extended velocity profile. Let us recall that all unstable modes have the largest possible radial extension. This radial stretching of non-axisymmetric modes during saturation appears to reduce the effects of phase mixing (by slowing the lengthscale shortening). In addition, the shear rate in the non-linear regime is significantly decreased and the timescale on which non-axisymmetric modes vanish thus becomes larger.

Non-axisymmetric modes participate in the generation of the non-linear axisymmetric flow. Clearly, three-dimensional simulations exhibit an enhanced axisymmetric kinetic energy, while the axisymmetric magnetic energy is approximately unchanged. The shear rate is also more rapidly decreased in 3D simulations.

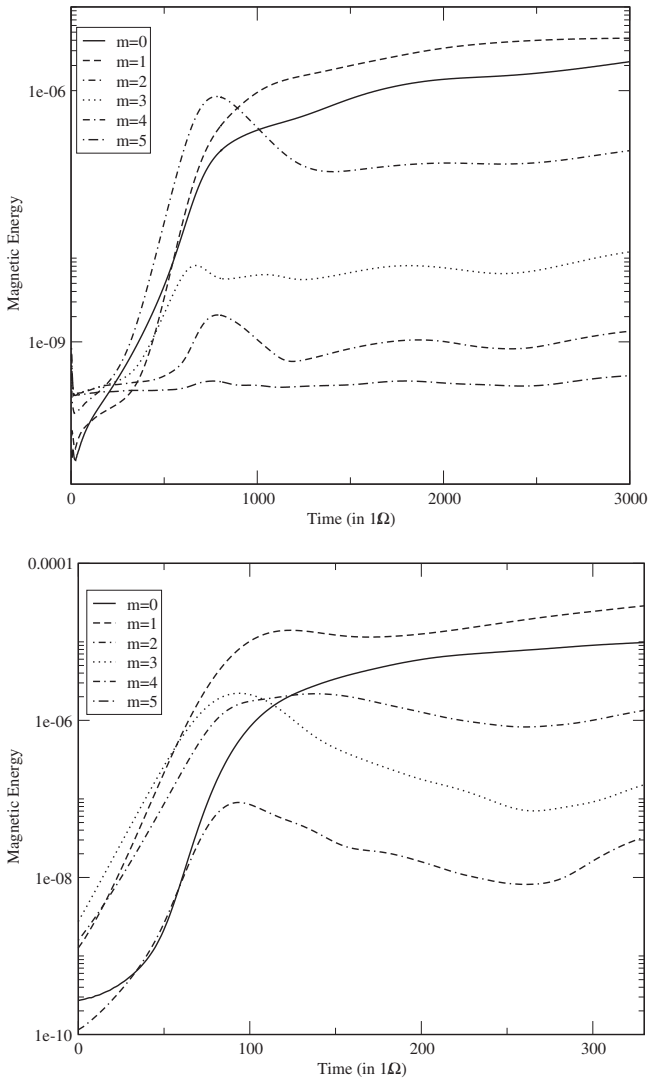

Fig. 11. Evolution of the magnetic energy for run R3 (top) and R5 (bottom).

6. Discussion

We have determined the impact of a background magnetic field having a toroidal component on axisymmetric disturbances. This additional component modifies the development of MS-MRI modes. Numerical simulations show that their exponential growth is associated with a axial drift. The axial drift velocity is directly proportional to the background toroidal component. Our local description allows to interpret the numerical results and to extrapolate them to the magnetostrophic regime. We have shown that axisymmetric MS-MRI modes could be affected by the presence of large-scale toroidal field. Our local description allows to extrapolate our results to a relevant parameter space for planetary interiors. In this regime, if the additional large-scale toroidal field is strong enough, the MS-MRI modes propagate axially whereas the growth rate is not substantially affected by the presence of the toroidal magnetic field.

In accretion disks, the axisymmetric MRI mode is always the most unstable mode. In addition, in sheared systems, non-axisymmetric modes end up to decay. However, we have shown that non-axisymmetric MS-MRI modes are relevant to planetary interiors according to our local linear theory. Whereas the background shear makes them only transient events, they are initially strongly amplified for a significant period of time. Our local analysis seems to account for the physical mechanism observed in the direct numerical simulations. The amplification rate of 3D MS-MRI modes depends crucially on the magnitude of the considered toroidal field. Curvature terms associated with the additional toroidal background field modify the structure of the modes in numerical simulations, characterized by a particular phase dependency. This particular structure appears as a signature of the MS-MRI in the planetary relevant regime. This result suggests that MS-MRI modes could be detectable in geodynamo simulations, but small enough Ekman numbers must be considered.

We have obtained excellent agreement between the local MS-MRI description and the global mode observed in the linear numerical results, it is however worth pondering on the possibility of an $m = 1$ Tayler mode (Tayler, 1973). This instability (relevant to stellar rather than planetary interiors) is however stabilized by rapid rotation (Pitts and Tayler, 1985; Ruediger and Schultz, 2010). Simulations performed in the absence of a background shear (vanishing Rossby number) were indeed stable. The Tayler instability can therefore only play a marginal role, if any, in our direct numerical simulations. The transition from the MS-MRI mode to the Tayler mode, for increasing background toroidal field, would deserve further studies and could be relevant to stellar interiors.

Our non-linear results may be relevant to the recent experimental results reported by Nornberg et al., 2010. The force balance in the PPPL experiment corresponds to a balance between the Coriolis and the Lorentz force ($\Lambda \approx \mathcal{O}(1)$). The authors interpret the obtained non-axisymmetric modes by the development of Magneto-Coriolis waves. They however note that the presence of non-axisymmetric modes, as opposed to axisymmetric modes, remains unclear. Our results could account for this unexpected observation. Our analysis can also be relevant to the traveling wave solutions observed in the Promise experiment (Stefani et al., 2006, 2008).

Because of the insulating outer boundary conditions, the axisymmetric toroidal field vanishes near the surface. As a result, the magnitude of this component inside Earth's outer core is undetectable by external probes. The toroidal field could be destabilizing if locally increasing outward faster than s (see the local dispersion relation above). Further numerical investigations are obviously needed. The presence of dominant non-axisymmetric MRI modes in the non-linear DNS presented in this manuscript however indicates a probable connection with these recent experimental results. Alternative explanations taking into account the influence of boundaries in such an experiment have been recently proposed by Gissinger et al. (2012).

We have highlighted the influence of different magnetic configurations on axisymmetric and non-axisymmetric MS-MRI modes. The magnitude of the large-scale toroidal field affects the axial drift velocity associated with growing modes as well as the structure of non-axisymmetric modes which take a helical structure. These results are of primary interest in order to understand the action of MS-MRI in planetary interiors. The model which is considered in this manuscript offer a finer description than the previous studies on MS-MRI (Petitdemange et al., 2008; Petitdemange, 2010) and the present study hopefully constitutes a first step towards a detection of MS-MRI modes in convection driven geodynamo simulations.

Appendix A. Details of the local analysis with curvature terms using shearing coordinates

We present here the local analysis, including curvature terms, as used in Section 4.2. Let us first consider the linearized equation for the radial component of the motion in the magnetostrophic balance

$$-2\Omega u_\phi = -\partial_s(p + V_{A\phi}b_\phi + V_{Az}b_z) + (\mathbf{V}_A\cdot\boldsymbol{\nabla})b_s - 2\frac{V_{A\phi}}{s}b_\phi. \quad (A.1)$$

In order to eliminate the pressure perturbation, we calculate d_z (A.1)

$$\begin{aligned} &-2\Omega\partial_z u_\phi = -d_s(F)\partial_\phi b_z - F\partial_s\partial_\phi b_z \\ &- V_{Az}\partial_s\partial_z b_z + (\mathbf{V}_A\cdot\boldsymbol{\nabla})\partial_z b_s - 2F\partial_z b_\phi, \end{aligned} \quad (A.2)$$

where $F = V_{A\phi}/s$.

The azimuthal component is

$$2\Omega u_s = -\frac{1}{s}\partial_\phi(p + V_{A\phi}b_\phi + V_{Az}b_z) + (\mathbf{V}_A\cdot\boldsymbol{\nabla})b_\phi + \frac{b_s}{s}\partial_s(sV_{A\phi}). \quad (A.3)$$

Combining ∂_z(A.3) and $s^{-1}\partial_\phi$(31) yields

$$2\Omega\partial_z u_s = -s^{-1}(\mathbf{V}_A\cdot\boldsymbol{\nabla})\partial_\phi b_z \quad (A.4)$$

$$+ (\mathbf{V}_A\cdot\boldsymbol{\nabla})\partial_z b_\phi + s^{-1}d_s(s^2F)\partial_z b_s. \quad (A.5)$$

The linearized induction equation affected by the curvature terms becomes

$$(\mathrm{d}_t - \eta D)b_s = (\mathbf{B}\cdot\boldsymbol{\nabla})u_s, \quad (A.6)$$

where $D = \partial_s(\partial_s + s^{-1}) + \frac{1}{s^2}\partial_\phi^2 + \partial_z^2$. The azimuthal component of the linearized induction equation is

$$(\mathrm{d}_t - \eta D)b_\phi = (\mathbf{B}\cdot\boldsymbol{\nabla})u_\phi + s\Omega' b_s - u_s s\frac{\mathrm{d}}{\mathrm{d}s}\left(\frac{B_\phi}{s}\right). \quad (A.7)$$

From Eqs. (A.6) and (A.7), we substitute u_s and u_ϕ respectively in (A.4) and (A.2). The component b_z is then expressed by using the condition $\mathbf{k}\cdot\mathbf{b} = 0$. This yields two coupled equations

$$\left[2\Omega i k_z s\Omega' - 2\Omega i k_z\frac{\mathrm{d}_t + \eta k_{tot}^2}{X}sF\prime - i\frac{mk_s}{k_z}XF' - i\frac{k_{sz}^2}{k_z}X^2\right]b_s =$$

$$\left(2\Omega i k_z(d_t + \eta k_{tot}^2) + i\frac{m^2}{sk_z}XF' + i\frac{m}{s}\frac{k_s}{k_z}X^2 - 2Fik_zX\right)b_\phi, \quad (A.8)$$

and

$$\Xi b_s = i\frac{k_{zm}^2}{k_z}X^2 b_\phi, \quad (A.9)$$

with the notations $X = i\mathbf{k}\cdot\mathbf{V_A}$, $F' = \mathrm{d}F/\mathrm{d}s = \mathrm{d}(V_{A\phi}/s)/\mathrm{d}s$ $k_{zm}^2 = m^2/s^2 + k_z^2$ and

$$\Xi = 2\Omega i k_z(\mathrm{d}_t + \eta k_{tot}^2) - i\frac{m}{s}\frac{k_s}{k_z}X^2 - i\frac{k_z}{s}Xd_s(s^2F). \quad (A.10)$$

Perturbations proportional to $\exp(ik_s s + im\phi/s + ik_z z)$ have been considered, where k_s depends on time. Taking the time derivative of Eq. (A.9) allows to express

$$\frac{\mathrm{d}b_\phi}{\mathrm{d}t} = -\frac{2\Omega k_z^2}{X^2k_{zm}^2}\eta\Omega' 2k_z m b_s + k_{zm}^{-2}s\Omega'\frac{m^2}{s^2}b_s - \frac{ik_z}{X^2k_{zm}^2}\Xi\frac{\mathrm{d}b_s}{\mathrm{d}t}. \quad (A.11)$$

We can now replace b_ϕ and $\mathrm{d}b_\phi/\mathrm{d}t$ in Eq. (A.8) and obtain an ODE for the variable b_s.

We restrict our attention to the magnetic configuration $F' = 0$ in order to avoid Acheson-type instabilities and focus on those induce by the shear. A study of the case $F'\neq 0$ is postponed to a future communication.

We then obtain

$$\begin{aligned} &\left[2\Omega i k_z s\Omega' - 2\Omega i k_z\frac{\mathrm{d}_t + \eta k_{tot}^2}{X}sF' - i\frac{mk_s}{k_z}XF' - i\frac{k_{sz}^2}{k_z}X^2\right]b_s \\ &= \left(2\Omega i k_z(\eta k_{tot}^2) + i\frac{m^2}{sk_z}XF' + i\frac{m}{s}\frac{k_s}{k_z}X^2 - 2Fik_zX\right) \\ &\times\left(\frac{-ik_z}{X^2k_{zm}^2}\right)\left(2\Omega i k_z(d_t - \eta D) - i\frac{m}{s}\frac{k_s}{k_z}X^2 - i\frac{k_z}{s}X(s^2F)'\right) \\ &b_s - 2\Omega i k_z\left(\frac{2\Omega k_z^2}{X^2k_{zm}^2}\eta\Omega'(2mk_s)b_s - s\Omega'\frac{m^2}{s^2k_{zm}^2}b_s\right. \\ &\left. + \frac{ik_z}{k_{zm}^2X^2}\left[2\Omega i k_z(d_t + \eta k_{tot}^2) - i\frac{m}{s}\frac{k_s}{k_z}X^2 - i\frac{k_z}{s}Xd_s(s^2F)\right]\frac{\mathrm{d}b_s}{\mathrm{d}t}\right), \end{aligned} \quad (A.12)$$

which yields (44).

References

Acheson, D.J., Hide, R., 1973. Rep. Prog. Phys. 36, 159–221.
Acheson, D.J., 1978. Philos. Trans. R. Soc. Lond. Ser. A 289 (1363), 459–500.
Balbus, S.A., Hawley, J.F., 1991. Astrophys. J. 376, 214–222.
Balbus, S.A., Hawley, J.F., 1998. Rev. Mod.. Phys. 70, 1–53.
Balbus, S.A., Hawley, J.F., 1992. Astrophys. J. 400, 610–621.
Dormy, E., Soward, A.M., 2007. Mathematical Aspects of Natural Dynamos. CRC Press.
Dormy, E., Cardin, P., Jault, D., 1998. Earth Planet Sci. Lett. 160, 15–30.
Fearn, D.R., 1993. In: Proctor, M.R.E., Matthews, P.C., Rucklidge, A.M. (Eds.), Solar and Planetary Dynamos. Cambridge University Press.
Gissinger, C., Ji, H., Goodman, J., 2012. Phys. Fluids 24, 074109.
Hollerbach, R., Rüdiger, G., 2005. Phys. Rev. Lett. 95, 124501.
Jones, C.A., Soward, A.M., Mussa, A.I., 2000. J. Fluid Mech. 405, 157–179.
Kitchatinov, L.L., Rüdiger, G., 2010. Astron. Astrophys. 513, 513L1.1–513L1.4.
Liu, W., Goodman, J., Herron, I., Ji, H., 2006. Phys. Rev. E. 74 (5), id. 056302.
Nornberg, M.D., Ji, H., Schartman, E., Roach, A., Goodman, J., 2010. Phys. Rev. Lett. 104, 074501.
Pessah, M.E., Psaltis, D., 2005. Astrophys. J. 628, 879–901.
Petitdemange, L., Dormy, E., Balbus, S.A., 2008. Geophys. Res. Lett. 35, L15305. http://dx.doi.org/10.1029/2008GL034395.
Petitdemange, L., 2010. Geophys. Astrophys. Fluids Dynam. 104, 287–299. http://dx.doi.org/10.1080/03091921003636496.
Roberts, P.H., Gubbins, D., 1986. Geomagnetism, vol. 2. London Academic Press.
Soward, A.M., Jones, C.A., 1983. Q.J. Mech. Appl. Math., 19–42.
Stefani, F., Gerberth, G., Gundrum, Th., Szklarski, J., Rüdiger, G., Hollerbach, R., 2008. Astron. Nachr. 329, 652–658.
Stefani, Gundrum, Gerbeth, Ruediger, Schultz, Szklarski, Hollerbach, 2006. Phys. Rev. Lett. 97, 184502.
Tayler, R.J., 1973. MNRAS 161, 365.
Pitts, E., Tayler, R.J., 1985. MNRAS 216, 139.
Ruediger, G., Schultz, M., 2010. Astron. Astrophys. 331, 121.
Terquem, C., Papaloizou, J.C.B., 1996. MNRAS 279, 767–784.